DOI: https://doi.org/10.1016/j.memsci.2023.121865

Development and hydrogen permeation of freeze-cast ceramic membrane

A. Gondolini[1], A. Bartoletti[1,2], E. Mercadelli[1,*], P. Gramazio[3,4], A. Fasolini[3,4], F. Basile[3,5,*], A. Sanson[1]

[1] National Research Council of Italy, Institute of Science, Technology and Sustainability for Ceramics (CNR-ISSMC, former ISTEC), Via Granarolo 64, 48018, Faenza, Italy

[2] Department of Chemical Sciences, Università degli Studi di Padova, Via Marzolo 1, 35131 Padova, Italy

[3] Department of Industrial Chemistry "Toso Montanari" University of Bologna, Viale del Risorgimento 4, 40136, Bologna, Italy

[4] Center for Chemical Catalysis - C[3], University of Bologna, Viale del Risorgimento 4, 40136, Bologna, Italy

[5] Consorzio interuniversitario per la scienza e tecnologia dei materiali (INSTM), Via G. Giusti, 9 50121 Firenze, Italy.

* Corresponding authors: elisa.mercadelli@istec.cnr.it; f.basile@unibo.it

Abstract

$BaCe_{0.65}Zr_{0.20}Y_{0.15}O_{3-\delta}$ - $Gd_{0.2}Ce_{0.8}O_{2-\delta}$ (BCZY-GDC) is currently one of the most investigated composites as ceramic membranes for H_2 separation and membrane reactors. In this context, we will present for the first time the possibility to exploit the ice-templating method coupled with screen printing to obtain hierarchically-structured proton-conducting ceramic membranes. All the processing steps to obtain a defect free dense/porous structure were considered and analysed. In particular, the formulation of screen printing ink was optimized in terms of nature/amount of deflocculant and type

of starting BCZY powder. An innovative membrane constituted by a 50 %-porous support with well-organized and aligned porosity and a 13 ± 3 μm thick dense layer on the top, was produced. The mechanical properties of this kind of structure, i.e. microhardness (452 ± 95 HV) and compressive strength (20.6 ± 5.6 MPa), were considered acceptable for practical applications. Promising H_2 fluxes of 0.36 and 0.42 mL min^{-1} cm^{-2} at 750°C, using a feed stream with 50 and 80% H_2 in He (H_2 %vol.) respectively, were obtained.

Keywords: BCZY-GDC, hydrogen permeation, ceramic membrane, freeze casting, screen printing, mechanical properties

1. Introduction

The hydrogen economy is a priority for the EU's post-COVID-19 economic recovery package guided by the European Green Deal. Hydrogen is in fact expected to play a pivotal role in a future climate-neutral economy, enabling emission-free transport, heating and industrial processes as well as energy storage as renewable carrier [1]. However the so called "green hydrogen" produced by zero-emission water electrolysis exploiting renewable electricity, represents only 5 % of the global hydrogen, being not yet as cost competitive as the one produced from natural gas/fossil fuels [2]. "Grey" and "blue hydrogen" obtained from the classical processes (i.e. hydrocarbon reforming and pyrolysis) contains inevitably CO_2, CO, H_2O, and other contaminants [3–7]. Thus, differently from H_2 produced by water electrolysis, the gases separation is a mandatory step to obtaining pure hydrogen through conventional technologies involving fossil fuels and C-based materials.

In this context, membrane technology, due to its many associated advantages such as simpler operation, higher modularity and adaptability with simpler up- and downscaling, compactness and lower capital, operating and maintenance costs, is an appealing candidate for hydrogen separation

[8], that can compete with highly cost and energy demanding traditional separation processes, i.e. cryogenic distillation and pressure swing adsorption. Specifically, ceramic hydrogen permeation membranes are cost-effective, robust, with high thermal and chemical stability at operating temperatures ranging between 300 and 1000 °C [9]. These characteristics make these membranes of particular interest for the possibility to combine separation process directly with catalytic reaction [10], e.g. for CO_2 hydrogenation reactions [11–13], leading to process intensification [14–16] and increasing the overall process efficiency.

Among the mixed proton and electron conducting membranes investigated so far, dense ceramic-ceramic composites of $BaCe_{0.65}Zr_{0.20}Y_{0.15}O_{3-\delta}$ and $Ce_{0.8}Gd_{0.2}O_{2-\delta}$ (BCZY-GDC) have shown suitable compatibility [15] and ambipolar conductivity [16], promising performances in terms of H_2 permeation [17,18], robustness in operation even in presence of CO_2 [19], and acceptable stability in H_2S containing atmospheres [20].

In a first approximation, the hydrogen obtained by the membrane is directly proportional to its thickness and therefore asymmetric membranes, a thin dense active layer supported onto a porous substrate, are preferred to minimize the resistance caused by bulk diffusion [21]. Nonetheless, other mechanisms become limiting in the H_2 separation upon reaching a characteristic membrane thickness, i.e., (i) catalytic surface exchange and (ii) gaseous transport [22]. In the case of asymmetric membranes, the optimization of the whole ceramic process is crucial to engineer the support porosity while obtaining a proper gas-tight thin layer on the top. In this direction, the fabrication methods selected must consider and solve all the technological issues arising from the coupling of a porous support with a dense active layer with extremely different microstructures.

With the aim of improving the membrane fabrication, freeze casting is considered a very attractive technique to obtain hierarchically-porous structures with aligned channels [23]. In particular, ice-templating consists in freezing a water-based ceramic slurry followed by the sublimation of the solvent and the final sintering of the green body, leading to highly porous and organized structures

with values of tortuosity close to the ideal case (τ=1), lower pressure drops, and higher gas permeability.

Despite the increasing research interest on this kind of structures for gas separation, only few papers have been published on mixed ionic–electronic conducting membranes just focused on oxygen separation, thus considering O^{2-}/electronic conducting materials [24,25].

In this study, the possibility to exploit the freeze-casting process to produce protonic-electronic conductive composite for hydrogen separation membranes will be presented for the first time. An innovative asymmetric BCZY-GDC membrane will be fabricated by a two-step process involving the production of a hierarchical porous support by freeze-casting and the deposition of a dense top-layer by screen printing. All the processing steps needed to obtain the asymmetric structure will be addressed. Finally, hydrogen permeation will be investigated as a function of temperature, composition of the feed stream and thickness of the porous support.

2. Experimental

BCZY-GDC membranes with a porous-dense architecture were obtained coupling the freeze casting process with screen-printing for the production of the porous support and the dense active layer respectively.

2.1. Production of the porous substrate

For the porous support, BCZY ($BaCe_{0.65}Zr_{0.20}Y_{0.15}O_{3-\delta}$, Marion Technologies, France) and GDC powders ($Gd_{0.2}Ce_{0.8}O_{2-\delta}$, FuelCellMaterials, USA) were mixed in 50:50 vol% with 1 wt% ZnO (Sigma Aldrich, Italy) as sintering aid. The detailed composition of the freeze casting slurry is reported elsewhere [26]. The slurry was poured in a circular crown silicon mould supported on metal plate and cooled at -40°C for 3 h in a freeze-drier (Lio 3000 PLT, 5Pascal, Italy) with a freezing rate of 30°C/h. The as-obtained freeze-cast support was then thermally treated and screen printed as detailed in 2.3.

2.2. Screen printing ink preparation for the dense layer

For the preparation of the dense layer two BCZY powders ($BaCe_{0.65}Zr_{0.20}Y_{0.15}O_{3-\delta}$, Marion Technologies, France) with specific surface area (SSA) of 4.92 m^2/g (d50 = 0.97 µm and d90 = 1.73 µm) and 13.4 m^2/g (d50 = 0.72 µm and d90 = 15.4 µm), were considered for the formulation of two different inks, namely ink A and ink B respectively. Each BCZY powder was previously mixed with GDC ($Gd_{0.2}Ce_{0.8}O_{2-\delta}$, SSA: 5.6 m^2/g, d50 = 0.49 µm and d90 = 2.17 µm, FuelCellMaterials, USA) in 50:50 vol% with 1 wt% ZnO (Sigma Aldrich, Italy). The powders' morphology and particles size distribution of the as-received commercial feedstocks (i.e. GDC and BCZY with different SSA values) is reported in Figure S1 and S2 respectively. For the inks production terpineol (Sigma Aldrich, Italy) was used as solvent. The type and amount of deflocculant was firstly optimized throughout viscosity analyses, fixing the powder/solvent volume ratio at 10 % as in the final ink compositions. The amount of deflocculant was calculated considering the different SSA of the two powders. The screen-printing inks were prepared at room temperature adding the deflocculant and powder to the solvent and mixing the suspension in a polyethylene jar with ZrO_2-based grinding beads. After 24 h of ball milling, ethyl cellulose (EC, 15-25 mPa · s, Sigma Aldrich, Italy) was added to the suspension as a binder and ball-milled for 3 h. The as-prepared inks were forced in a three-roll mill (Exakt 80E, Norderstedt, Germany) [27,28] to obtain a more homogeneous and structured system.

2.3.Production of porous-dense bilayer

The porous supports produced in 2.1 were demoulded and thermally treated at 1200°C for 2h. The pre-sintered samples were then screen-printed using a 165-mesh screen and dried in IR furnace at 80°C for 30 min. The deposited samples were finally sintered at 1600°C for 4 hours obtaining membranes of 15 mm in diameter with final thicknesses of 2.00 and 0.85 mm (named as Mbr2.00 and Mbr0.85 respectively). The final thickness of the membranes was tailored by grinding down the porous side.

2.4. Characterization

The best type and amount of deflocculant were determined by viscosity test at a controlled temperature of 25 °C using a controlled-stress rheometer (Bohlin CVOR 120, Malvern Instruments,

Italy) with 20 mm diameter parallel-plate geometry, setting a gap between plates of 0.5 mm. The flow curves of the suspensions were determined applying a shear stress from 0.01 to 100 Pa.

The phase purity of the obtained membranes was assessed through X-Ray diffractometer (D8 Discover X-Ray diffractometer, Bruker Cu Kα radiation, Germany) and microstructures were investigated using optical digital microscope (RH-2000, Hirox, France) and scanning electron microscopy (Field Emission Gun - Scanning Electron Microscopy, FEG-SEM, ΣIGMA, Zeiss, Germany). To evaluate the cross section of the sintered membrane, each sample was embedded in epoxy resin, cut with a cutting machine and then mechanically polished up to 0.25 µm finishing. The grain dimension was estimated by Image Analysis using ImageJ software considering multiple SEM surface micrographs.

The open porosity (%) of the freeze cast substrates were determined according to ISO/DIS 10545-3:1993 through water absorption. The results were compared to the ones obtained using mercury intrusion technique (Thermo Finningan Pascal 140) working at pressure from ambient to 400 kPa.

The compressive strength of the sintered samples was investigated with a Universal Testing Machine (Zwick/Roell Z050, Germany) considering cylindrical samples with a high/diameter ratio of about 0.5 using a crosshead speed of 2 mm/min.

Membranes leak rate was tested employing the same reactor used for H_2 permeation, as described hereafter. Leak rate was tested at room temperature, using a polymeric hand-carved o-ring, a commercial septum (CrossLab non-stick BTO inlet septa), a mixture of 50% of H_2 in He (H_2 %vol.) as feed stream, and Ar as sweep stream observing the amount of leaked feed gas in the sweep current. To develop a robust testing procedure, preliminary tests with non-permeable alumina disks were carried out, showing no leaked gas. Membranes gas tightness was considered acceptable with values of leaked He inferior to 0.5 %.

Before determining membrane permeation performances, both surfaces of the membrane were activated with Pt. Tetraammineplatinum(II) nitrate (Premion®, 99.99%) solution, with the suitable concentration, was deposited on the membrane surfaces and then dried in oven at 50°C for 1 h to

obtain a total Pt (metal) amount of 0.23 mg and 2.3 mg on the dense and porous side respectively. Reduction of Pt precursor to metal Pt was carried out directly in the reactor set-up during the sealing procedure and just before the permeation testing.

Permeation measurements were carried out on disk shaped samples with a diameter of about 15 mm determining hydrogen permeation in a temperature range from 350 to 750 °C. The set-up employed for measurement is composed of a handmade double chamber quartz reactor, where feed and sweep sections are separate. Sealing is achieved using silver alloy rings and keeping the reactor at 750°C for 24 h to achieve acceptable condition of leakage. A mixture of H_2 and He were employed as feed gas, while pure Ar was used as sweep gas. All gaseous current were controlled by mass flow (MFC) and the flow rate were 80 mL/min and 150 mL/min for feed and sweep gas respectively. Both current were humidified to saturation at 28 °C. Hydrogen concentration in permeate gas was determined using an Agilent Technologies 490 Micro GC equipped with a Molsieve5A capillary module. An appropriate sealing was determined by monitoring He content at the permeate side, and results were considered acceptable when He leaked was below 5%, and leaked hydrogen was subtracted form permeation results. Data reported in the present study were recorded at a steady state after 30 minutes of stabilization. Temperature was monitored by a thermocouple close to the membrane. Each permeation point was the result of 15 analysis. The activation energy for H_2 permeation was calculated by the Arrhenius equation:

Eq. 1 $$J = J_0 \exp\left(\frac{-E}{RT}\right)$$

By plotting ln(*J*) as a function of *1/T*, the slope can be used to obtain the activation energy.

3. Results and discussion

3.1 Production and characterization of the membrane

The porous support was obtained following the optimized composition and procedure reported in [26]. As described in the Experimental section, the freeze cast supports were firstly thermally treated at 1200°C for 2h to deposit the dense active layer by screen printing, thus obtaining the porous-dense BCZY-GDC membrane.

Suitable screen-printing inks were formulated choosing the optimal type and amount of deflocculant agents, considering a powder/solvent volume ratio of 10 %. The stability of the BCZY-GDC powder in the ink is, in fact, strongly connected to effectiveness of the coordination sphere around particles. The latter acts on the particles through one or two mechanisms eventually combined: electrostatic repulsion or steric stabilization [29]. Among the dispersants chosen, Glycerol Trioleate (GTO) shows a prevailing steric effect, furoic acid (FA) presents mainly an electrostatic activity while Lauric acid (LA) shows a combination of electrostatic and steric behaviour. Viscometry has been considered to select the most effective dispersant for the system [30].

Different dispersant amounts (g/m^2 of ceramic powder) were tested in the range between 5×10^{-4} to 1×10^{-2}. Some viscosity/shear stress curves of the suspension containing different amounts and type of deflocculant compared to the bare BCZY-GDC/terpineol system are reported as example in Figure 1.

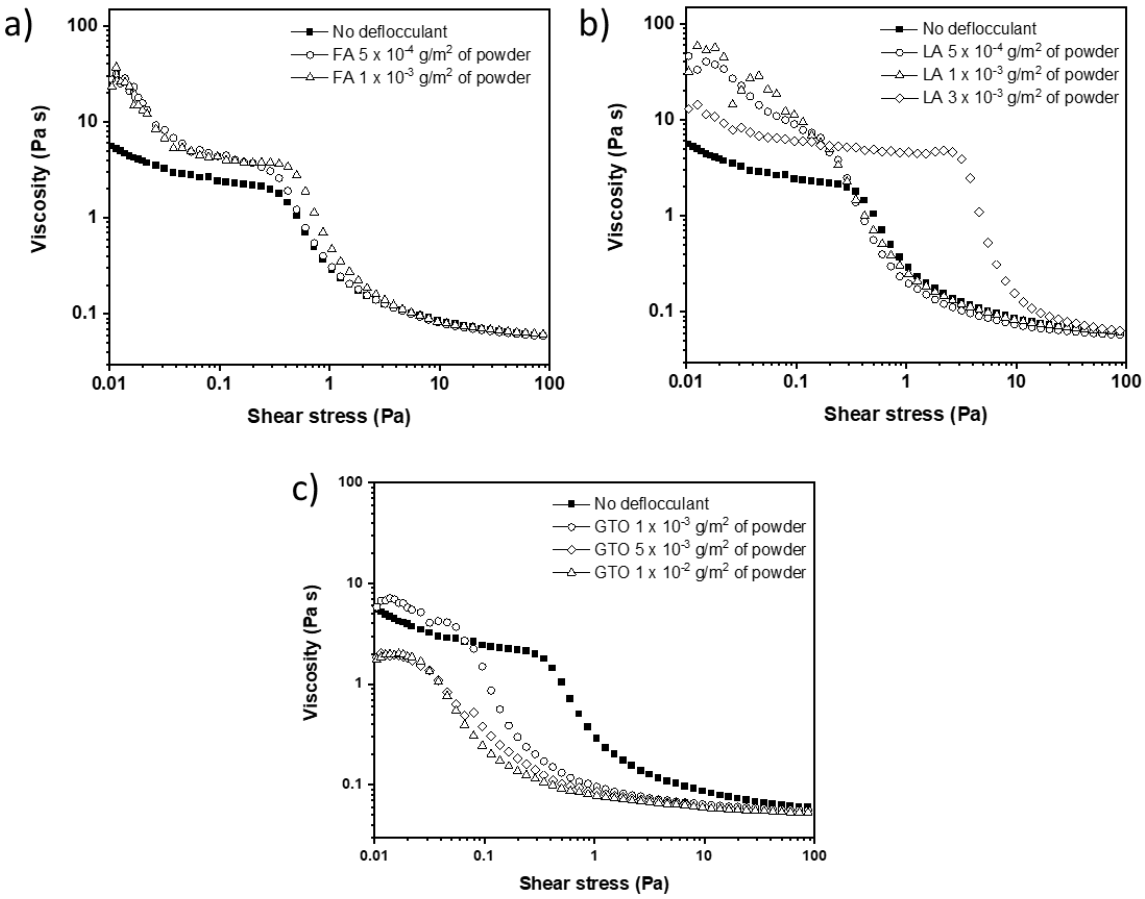

Figure 1. Viscosity/shear stress curves of the BCZY-GDC suspensions containing different amount of furoic acid a), lauric acid b) and glycerol trioleate c).

The registered viscosity curves show a pseudoplastic behaviour for all the considered slurries and the lowest viscosity values were recorded for suspensions containing GTO. The values of suspension viscosity as a function of different deflocculant concentrations, recorded at shear stress of 1 Pa (value of shear to which an ink is typically subjected in the printing process), are reported in Figure 2. The results confirm that the deflocculants having mainly or partially an electrostatic behaviour (LA and FA) do not show a stabilizing effect for the suspensions. On the other hand, the prevailing steric stabilization acted by GTO is the most effective mechanism to stabilize the ink, in particular at concentrations equal to or greater than $1x10^{-3}$ g/m^2 of dispersant. This GTO concentration was therefore selected for the production of BCZY-GDC screen printing inks.

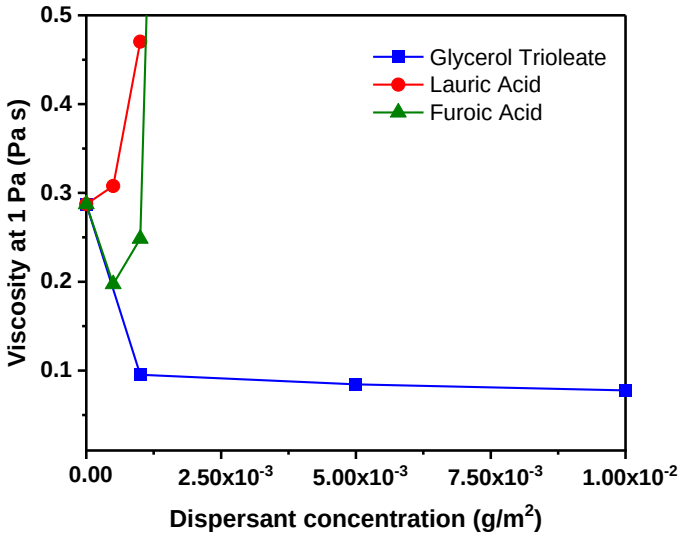

Figure 2. Viscosity of BCZY-GDC/terpineol suspensions produced using different types and amounts of deflocculants measured at 1 Pa.

The influence of the specific surface area (SSA) of the starting BCZY powder on the microstructure of the final dense membrane layer was also investigated. The use of finer powder with higher specific surface area and thus a higher sintering activity, could in fact promote the densification of the screen printed active layer at lower temperatures [21]. For this reason, Ink_A and Ink_B were produced using BCZY-GDC powder as reported in the Experimental section considering BCZY commercial powders with different SSA values of 4.92 and 13.4 m^2/g respectively, according to the formulations reported in Table 1.

Table 1. Inks compositions (expressed in vol%) formulated using BCZY powder with lower (Ink_A) and higher (Ink_B) specific surface area.

Component	Ink_A	Ink_B
BCZY-GDC	8.5	8.5
Terpineol	85.1	84
GTO	1.3	2.5

EC	5.1	5.0

Both the inks were screen printed on the freeze-cast porous supports thermally treated at 1200°C for 2h. The as-produced membrane systems were finally sintered at 1600°C for 4 hours to obtain the complete membranes with the porous-dense structure.

Figure 3 shows the microstructure of the membrane porous support obtained after the final sintering step, while the values of open porosity measured using Hg intrusion technique (Hg) and following the ISO/DIS 10545-3:1993 procedure (ISO) are reported in Table 2. The SEM micrographs confirm the obtaining of a membrane constituted by a porous support with vertically-oriented pores and high level of open porosity as demonstrated by porosimetric analyses. These results are consisted with the ones reported in our previous work [26].

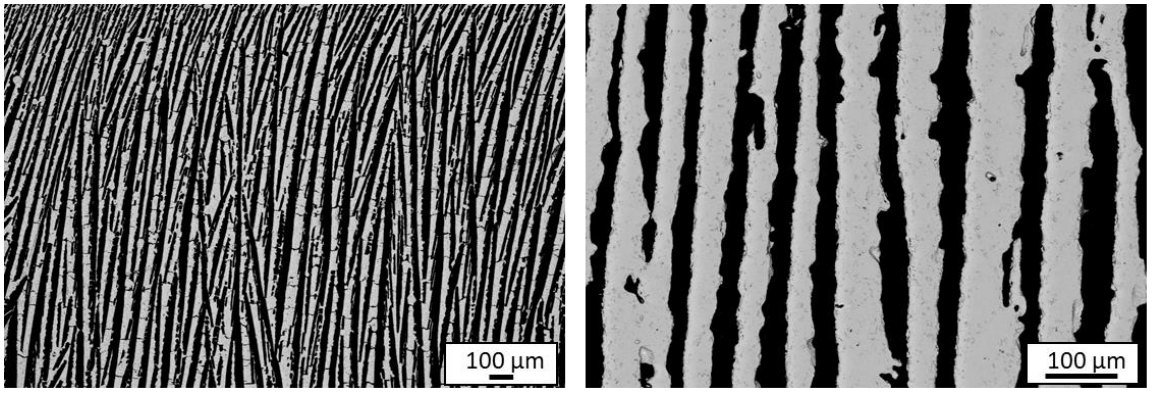

Figure 3. SEM micrograph of the polished cross section (support side) of the final membrane at different magnifications.

Table 2. Total open porosity obtained using Hg intrusion technique (Hg) and following the ISO/DIS 10545-3:1993 procedure (ISO) for the membrane support sintered at 1600°C for 4 hours.

Sample	**Total open porosity $_{Hg}$ (%)**	**Total open porosity $_{ISO}$ (%)**
Support	51.3 ± 08	49.4 ± 1.7

The XRD diffractogram of the dense membrane layer (Figure 4) shows the maintenance of pure BCZY-GDC phases indicating that the whole process did not affect the stability of the dual perovkite-fluorite phases.

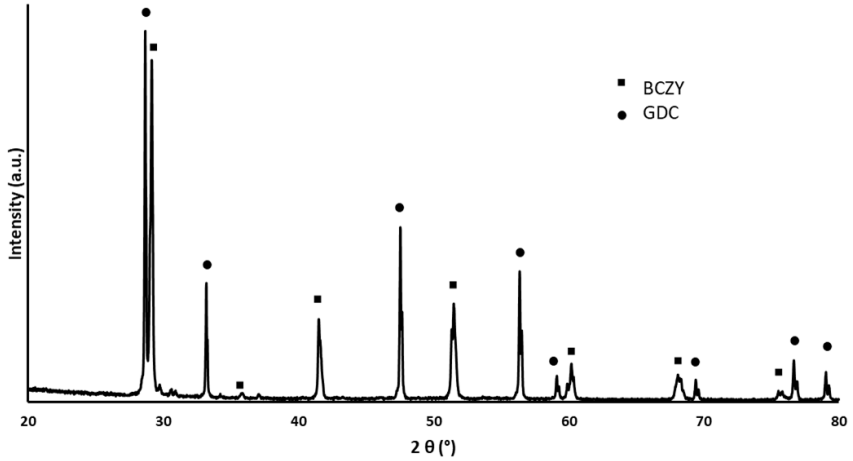

Figure 4. XRD analysis of the dense BCZY-GDC membrane surface sintered at 1600°C for 4 hours.

The SEM micrographs of the cross sections and dense membrane surfaces of the samples deposited with Ink_A and Ink_B were reported in Figure 5 and 6, respectively.

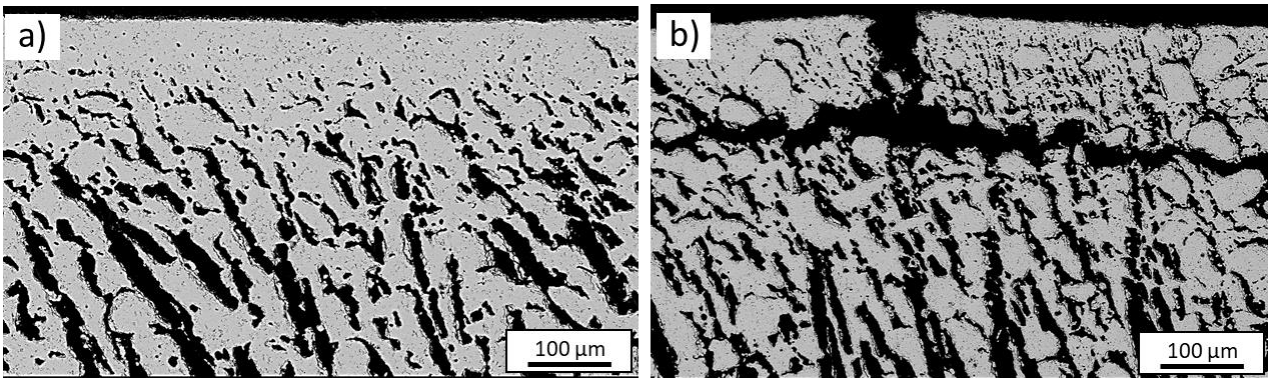

Figure 5. SEM micrographs of the polished cross section of the membranes deposited with Ink_A a), and Ink_B b).

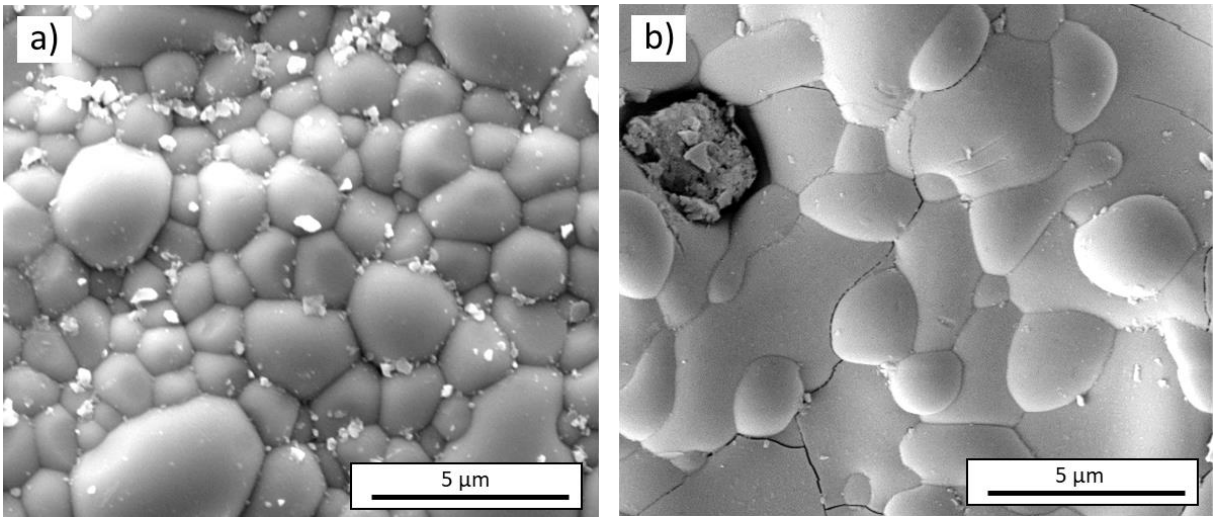

Figure 6. SEM micrographs of the screen-printed dense surface of the membranes deposited with Ink_A a), and Ink_B b).

As clearly shown by the SEM images, the dense active layer produced with Ink_B shows a relevant number of cracks in both cross section and top surface (Fig. 5b and 6b). This is attributed to an unsuitable particle size distribution and an insufficient green density of the printed layer. The BCZY powder used in Ink B is, in fact, characterized by a combination of inhomogeneous particle size (Figure S1 and S2) and high SSA (13.4 m^2/g) causing anisotropic shrinkage of the screen printed layer and incompatible shrinkage mismatch between the freeze cast support and the deposited film. This leads to the final delamination and detachment (Fig. 5b) of the dense layer from the substrate during sintering. Moreover, the use of a finer powder (Ink_B) promotes the coarsening of BCZY grains as shown in Figure 6. On the contrary, no defects and a good level of densification of the membrane layer were achieved for samples produced using the Ink_A (Fig. 5a and 6a). A mean grain size of 1.86 ± 0.73 µm was calculated from image analysis of SEM micrograph collected for the dense layer surface.

For these reasons, the Ink_A was selected for the production of hierarchically-structured BCZY-GDC membranes for the further mechanical and functional tests. Membranes constituted by a porous support with two different thicknesses (i.e. 2.00 mm and 0.85 mm, named as Mbr2.00 and Mbr0.85 respectively) were successfully produced as depicted in Figure 7a. A typical cross-section

274 microstructure of a hierarchically-structured membrane obtained using the optimized ceramic process
275 is reported in Figure 7b. A 13 ± 3 μm thick dense layer with residual porosity of 1.5 ± 0.9 % was
276 obtained.

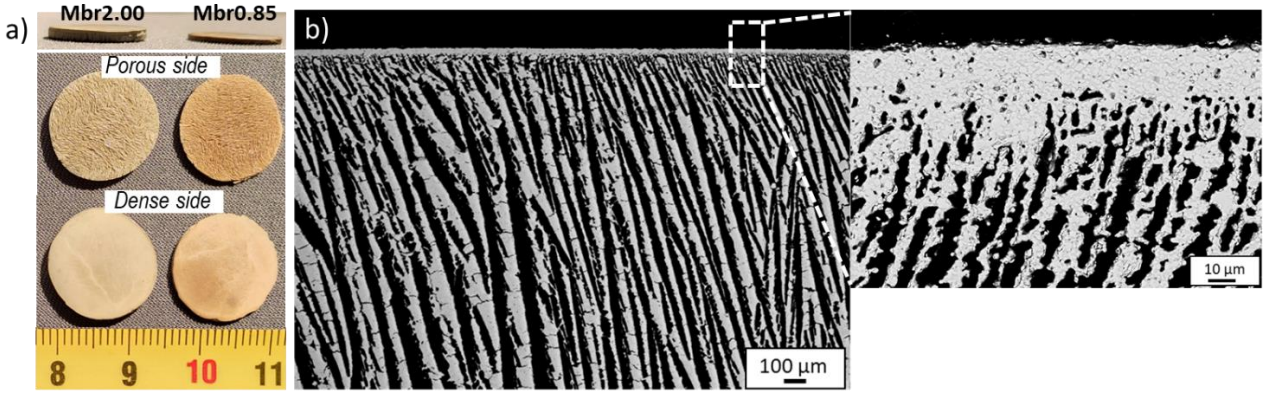

277

278 **Figure 7.** a) Photographs of the screen printed/freeze cast membranes with different thicknesses. b)
279 SEM micrographs, at different magnifications, of the polished cross section of the hierarchically-
280 structured BCZY-GDC membrane.

281

282 To investigate the mechanical properties of the produced membranes, compression tests were
283 performed on the as-produced samples. A compressive strength (σ) value of 20.6 ± 5.6 MPa was
284 registered for the hierarchically-structured BCZY-GDC membrane, acceptable for the subsequent
285 permeation tests. In addition, σ value is comparable to the one recorded on the freeze cast porous
286 support reported in [26] underlining that the contribution of the dense layer to the mechanical strength
287 of the asymmetric membrane is practically negligible.

288

289

290 **3.2 Hydrogen permeation measurements**

291 The hydrogen permeability of the produced membranes was characterized at high temperature and
292 different hydrogen partial pressures. The characteristics of the two tested membranes (Mbr2.00 and
293 Mbr0.85) are summarized in Table 3.

294

Table 3. Characteristics of the hierarchically-structured BCZY-GDC membranes considered for hydrogen permeation tests.

Sample	Membrane thickness (mm)	Total open porosity $_{ISO}$ (%)	Dense layer thickness (µm)	Residual porosity (%)
Mbr0.85	0.85 ± 0.01	49.8 ± 2.2	13.0 ± 1.0	1.5 ± 0.7
Mbr2.00	2.00 ± 0.01	51.9 ± 1.1	14.5 ± 1.5	1.3 ± 0.7

The membranes were activated with Pt to favour both hydrogen activation and water splitting reaction and to avoid surface kinetic effects on permeation [22,31,32].

Figure 8 shows permeation curves for the thicker Mrb2.00 membrane. Generally, the hydrogen flux through a mixed proton–electron conducting membrane is described by the Wagner equation, which is reported hereafter (Eq. 2):

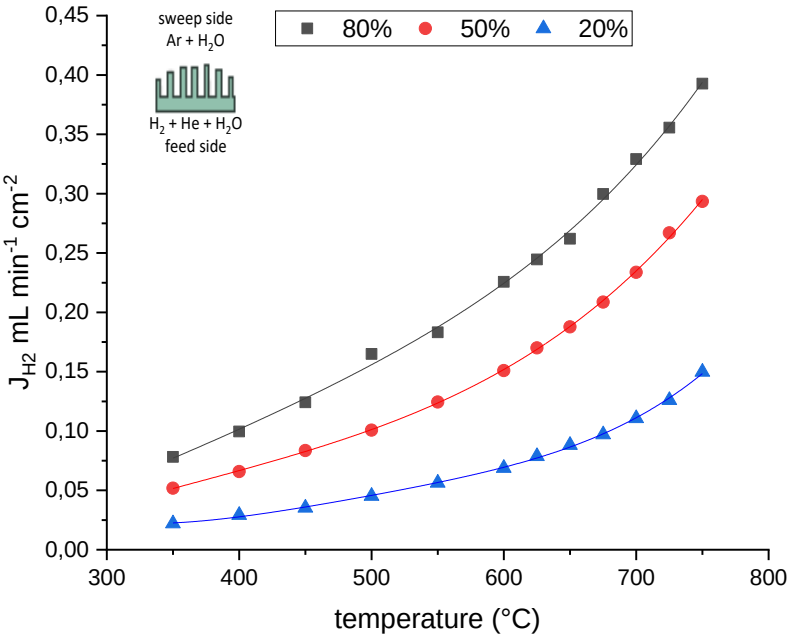

Figure 8. H_2 fluxes (mL min^{-1} cm^{-2}) as a function of temperature and composition of the feed stream (80%, 50% and 20% H_2 in He, H_2 %vol) for a 2 mm thick membrane (Mbr2.00). Both feed

and sweep streams are humidified to saturation at 28°C. Insert on top shows a schematic of the membrane test configuration.

Eq. 2 $$J_{H2} \approx \frac{RT}{4F^2L}\frac{(\sigma_{H^+}+\sigma_{O^{2-}})(\sigma_e+\sigma_h)}{\sigma_T} ln\frac{p(H_2\ feed)}{p(H_2\ sweep)}$$

Where σ_j and σ_T are, respectively, partial conductivity of *j* species and total conductivity and *L* is the thickness of the dense mixed conductor. According to this equation and in line with the obtained result the permeated hydrogen increases with an increase of the operating temperature thanks to a higher ion mobility in the ceramic system. Moreover, it raises with an increase in hydrogen concentration at the retentate side due to an increased driving force given by the hydrogen partial pressure in the feed. In fact, in each curve registered for different H_2 compositions (80%, 50% and 20% H_2 in He, H_2 %vol.) an increment of J_{H_2} is observed when the temperature is increased from 350 to 750 °C. However, it must be noted that at high temperatures (>650 °C) the amount of hydrogen in the permeated flux is also increased by the water splitting reaction of steam molecules present at the retentate (feed side). Water splitting contribution can be seen as an apparent permeation that nevertheless allows to increase the amount of separated hydrogen. In the water splitting process, a molecule of water reacts over the Pt sites of the membrane producing H_2 (at the permeate) and a surface oxygen that in turn is adsorbed, splitted in O^{2-} ions and migrates back through the dense layer reaching the retentate. Oxygen ions reacts with the fed hydrogen producing steam. The net result is the consumption of hydrogen at the feed giving H_2O and the production of H_2 at the permeate consuming H_2O giving what can be called an apparent hydrogen permeation as the real permeated species is the surface oxygen and not hydrogen. This results in a further increase in hydrogen separation at high temperature as it can be seen from the results obtained above 650 °C.

The highest J_{H_2} value was obtained at 750 °C, with a composition of 80% H_2 in He, reporting 0.39 mL min^{-1} cm^{-2}, while an H_2 flux of 0.29 mL min^{-1} cm^{-2} was achieved using 50% H_2 in He as feed gas.

Post-mortem analyses, shown in Supplementary Material, evidenced that neither structural (Figure S3) nor morphological modifications (Figure S4) occur after permeation tests.

3.2.1 Influence of membrane thickness

Asymmetric architectures are used to couple a mechanically stable porous architecture with a thin dense layer, decreasing, in this way, the thickness (L) of the active dense membrane part and thus increasing permeation [33]. In such systems, the porous layer serves as a mechanical support for the thin active dense layer to confer the necessary mechanical stability to the entire system. However the porosity of the support must be properly engineered to minimize mass transfer resistance [34,35] and to eventually facilitate its activation with a specific catalyst.

To understand the influence of the porous support thickness on final hydrogen permeation, membranes having the comparable dense layer thickness but different porous support thicknesses (2.00 mm and 0.85 mm, named as Mbr2.00 and Mbr0.85) were considered. Results of Mbr2.00 and Mbr0.85 permeation performances are reported in Figure 9.

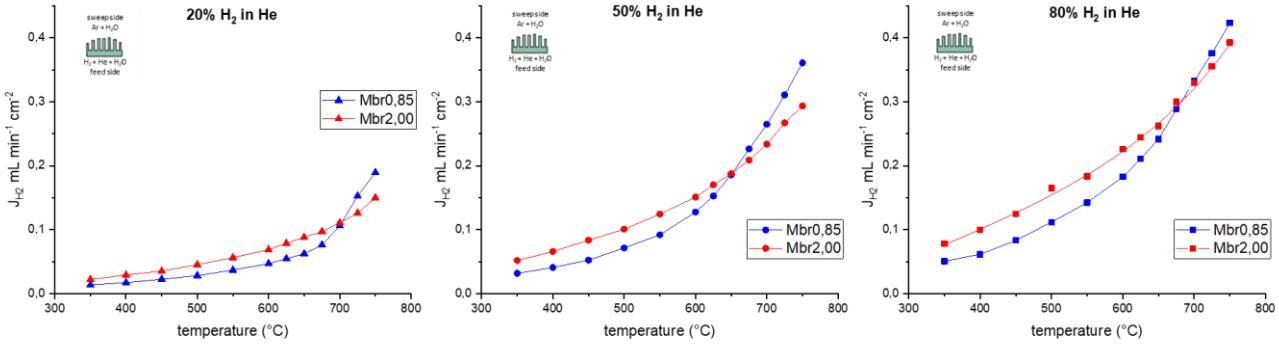

Figure 9. H_2 permeation fluxes as a function of temperature and composition of feed streams for Mbr0.85 (blue) and Mbr2.00 (red) membranes. The inset shows a schematic of the membrane test configuration.

Also in this case, the temperature was varied from 350 to 750 °C and three compositions of feed streams were investigated: 80%, 50% and 20% (H_2 %vol). For both samples an increase in

temperature and hydrogen pressure corresponds to an increase in the permeated hydrogen as expected from Wagner equation and water splitting contribution. When J_{H2} performances of the two membranes were compared some interesting information arose. It is possible to observe that for every feed stream composition, Mbr2.00 shows slightly higher J_{H2} at temperatures lower than 700 °C, while this tendency inverted at 750°C, where Mbr0.85 membrane shows a sharp increase in permeation values. This is consistent with a different extent of the already discussed two separation phenomena occurring in Pt-activated BCZY-GDC based membranes: (1) transport of protons and electrons through the dense layer, (2) water splitting reaction in the sweep side, due to oxide-ion conduction of the composite at temperatures higher than 650°C [35–39]. The latter phenomenon is related to the presence of Pt along the porous matrix. At lower temperatures, hydrogen permeation through the dense layer is the predominant phenomenon while, at higher temperatures, water splitting contributes to larger extent.

Thus, the sharp increase in Mbr0.85 permeation curve, at temperature > 700 °C, can be attributed to the Pt sites close to the dense layer, causing a more efficient O^{2-} transport and thus enhancing the water splitting reaction rate in the thinner membrane. This is attributed to the major "dilution" (i.e. lower concentration) of the Pt particles in the Mbr2.00 porous substrate (Figure S5 b) in respect to the Mbr0.85 one (Figure S5 a), considering the same Pt loading used for the two different samples. The higher thickness of the Mbr2.00 implies, in fact, that a significant amount of the Pt is more distant from the dense side or at least less concentrated (considering an equal Pt penetration depth) in respect to the Mbr0.85, requiring O^{2-} to be transported across a greater portion of the porous matrix. On the contrary, a higher concentration of Pt particles closer to the dense side is observed for Mbr0.85 (Figure S5 a) compared to Mbr2.00 (Figure S5 b). This positively affects the transport phenomena constraints in the case of the Mbr0.85 for water splitting reaction. On the other hand, permeation performances obtained at temperatures < 600 °C, which primarily depend on proton and electron transfer through the dense active layer, correlate in a complex way with average thickness, residual porosity (Table 4) but also surface roughness, and sample homogeneity in terms of defects and

microstructure. For these reasons we believe that the slightly higher permeation flux observed for Mbr2.00 in the 350-650 °C range might be due to an overall thinner and/or denser active layer in respect to Mbr0.85. Unfortunately, the standard deviation of the morphological parameters (thickness/residual porosity) of the dense layers of the 2 membranes does not allow to discern a precise morphology-permeation correlation. More accurate investigations of the microstructure (i.e. through micro-CT techniques) will be carried out to further study and investigate this trend at low temperatures.

Indication of a different water splitting behaviour by the two systems was further evident when the results were plotted as percent increase in permeation between J_{H2} values recorded at 500 °C (where water splitting is negligible) and at 750°C. From calculation carried out on data recorded with 50% H_2 in He (H_2 %vol) it is possible to notice a higher increase in the hydrogen permeation from 500 to 750 °C as reported in equation 3 and 4:

Eq. 3 $$\text{Mbr0.85}\Delta\% = \frac{J_{H_2 750-500°C}}{J_{H_2 750°C}} = 80\%;$$

Eq. 4 $$\text{Mbr2.00}\Delta\% = \frac{J_{H_2 750-500°C}}{J_{H_2 750°C}} = 66\%$$

To further investigate the effect of membrane architecture and porous layer thickness on the phenomena occurring during H_2 permeation, streams fluxes were inverted, sending feed current on the membranes porous side (Inverse Fluxed, I.F.), while at the dense side was fluxed the sweep stream (where water splitting takes place). The tests were performed on the same membrane and the inlet permeate and retentate flows were exchanged to obtain the flows inversion. The results of the permeation tests with inverse fluxed (I.F.) are shown in Figure 10 and compared with the ones of the standard configuration (S.F.).

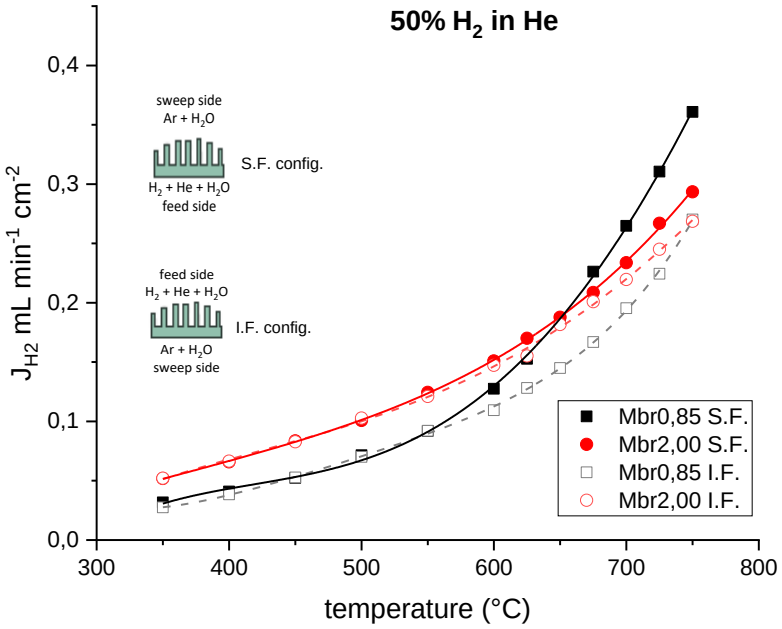

404

405 **Figure 10.** H_2 fluxes (mL min^{-1} cm^{-2}) as a function of temperature. Measurements were performed
406 in both configurations: i) feeding with 50% H_2 in He (H_2 %vol) the porous support (configuration
407 I.F.) and, ii) feeding with 50% H_2 in He (H_2 %vol) the dense side (configuration S.F.). The inset
408 shows a schematic representation of the membrane test configuration.

409

410 For both membranes, at temperatures below 600°C, changing the feed stream from the dense side
411 (standard fluxes, S.F. config.) to the porous side (inverted fluxes, I.F. config.) does not result in
412 different J_{H2} values. On the opposite, at higher temperature (> 600°C), a different permeation between
413 the two configurations is observed particularly for Mbr0.85, with an increase in permeation when the
414 permeate is sent to the porous side. It must be noted that the Pt amount at the porous side is 10 times
415 higher than on the dense side. Thus, the systems should catalyse water splitting to a higher extent
416 when tested in the standard configuration, where the humid sweep is sent over the porous support.
417 This is the case of Mbr0.85. On the opposite, similar curves are recorded for standard and reverse
418 flow over Mbr2.00 where the change of side and thus of Pt amount seems to have a slight effect. This
419 phenomenon can be attributed to both the low Pt particles concentration in the thicker porous support

and the presence of mass transfer limitations. In fact, porosity, though well oriented, may result in concentration polarization effect. An interesting study showed that concentration polarization can be avoided for uniform freeze casted pores with average pore diameter higher than 20 microns [24]. The membranes here reported are characterized by average pore diameters lower than this value, as can be seen from SEM images reported in Figure S5. Thus, performance limitation due to concentration polarization effect may occur.

Finally, the apparent activation energies of the two membranes were calculated to get further insights into the contribution to permeation of the different phenomena (Table 4). The apparent activation energies calculated for Mbr0.85 and Mbr2.00 (respectively 0.24 and 0.20 eV at T < 625 °C and 0.54 and 0.35 eV at T > 625 °C) are comparable with those of other dense ceramic membranes present in literature (Table 4). The membranes show two different activation energies in the temperature range below and above 625°C. This difference has been already reported in literature [18] and is due to the prevalence of different transport mechanisms as already discussed above. A higher activation energy is related to the prevailing oxygen ion transport followed by water splitting at T>625°C, while the decrease in activation energy at lower temperatures is due to a higher contribution of proton transfer through the membrane.

Table 4. Apparent activation energies reported in literature for dense ceramic membranes.

System	Architecture	Configuration	Activation Energy (eV) – low T	Activation Energy (eV) – high T	Ref.
Mbr0.85 - $BaCe_{0.65}Zr_{0.20}Y_{0.15}O_{3-\delta}$ (BCZY)–$Gd_{0.2}Ce_{0.8}O_{2-\delta}$ (GDC) - *(BCZY-GDC)*	Disk	Dual-phase – asymmetric	0.24	0.54	This work
Mbr2.00 - $BaCe_{0.65}Zr_{0.20}Y_{0.15}O_{3-\delta}$ (BCZY)–$Gd_{0.2}Ce_{0.8}O_{2-\delta}$ (GDC) - *(BCZY-GDC)*	Disk	Dual-phase – asymmetric	0.20	0.35	This work
$SrCe_{0.7}Zr_{0.2}Eu_{0.1}O_{3-\delta}$ *– NiO-$SrCe_{0.8}Zr_{0.2}O_{3-\delta}$*	tubular	Single-phase – asymmetric	not reported	0.84	[40]
$Sr(Ce_{0.6}Zr_{0.4})_{0.85}Y_{0.15}O_{3-\delta}$ (SCZY)–*SCZY-NiO*	Disk	Single-phase – asymmetric	0.32	0.50	[41]

$BaCe_{0.65}Zr_{0.2}Y_{0.15}O_{3-\delta}$ (BCZ20Y15) -$Ce_{0.85}Gd_{0.15}O_{2-\delta}$ (GDC15)	Disk	Dual-phase – symmetric	0.82	1.04	[16]
$SrCe_{0.95}Tm_{0.05}O_{3-\delta}$ (SCTm) – *SCTm*	Disk	Single-phase – asymmetric	1.35	0.182	[42]
$SrCe_{0.95}Y_{0.05}O_{3-\delta}$ (SCY) – *SCY*	Disk	Single-phase – asymmetric	not reported	1.11	[43]
$La_{0.5}Ce_{0.5}O_{2-\delta}$ (LDC) – *LDC*	disk	Single-phase – asymmetric	not reported	1.219	[44]

The hierarchically-structured BCZY-GDC membranes presented in this work show hydrogen performances comparable to the ones recorded for tape cast asymmetric BCZY-GDC membranes [17] that are, up to now, among the highest reported in literature for ceramic-based membranes (Table 5). Further work will be necessary to carefully investigate and compare the morphological and microstructural features (such as tortuosity, average pore opening diameter, specific surface area, porosity, etc.) of the porous supports obtained via conventional tape-casting and freeze casting. Besides the morphological/microstructural optimization (such as thickness and densification level) of the thin active layer, these results will be of paramount importance for the construction of models to effectively identify the predominant key-parameters (i.e. material properties, catalysts, microstructural properties and operational conditions) to improve H_2 permeation of ceramic membranes. However, the results presented in this paper for the first time, lay the foundation for further studies on the development of ceramic-based membranes using non-conventional technique for the production of hierarchically engineered porosity.

Table 5. Hydrogen separation performances for ceramic membranes reported in literature. Bold systems indicate the active (dense) layer whereas italics is used for the porous support.

System	Architecture	Configuration	Dense layer Thickness [mm]	J [mL cm^{-2} min^{-1}]	Feed/Sweep gasses	T [°C]	Ref.
Cerate-zirconate-based							
$SrCe_{0.7}Zr_{0.2}Eu_{0.1}O_{3-\delta}$ – *NiO-$SrCe_{0.8}Zr_{0.2}O_{3-\delta}$*	tubular	Single-phase – asymmetric	0.033	0.23	100% H_2	900	[40] [45]
$Sr(Ce_{0.6}Zr_{0.4})_{0.85}Y_{0.15}O_{3-\delta}$ (SCZY)–*SCZY-NiO*	disk	Single-phase – asymmetric	0.017	0.184 mmol cm^{-2} min^{-1}	100% H_2	800	[41]
$BaCe_{0.65}Zr_{0.20}Y_{0.15}O_{3-\delta}$ (BCZY)–$Gd_{0.2}Ce_{0.8}O_{2-\delta}$ (GDC) - *(BCZY-GDC)*	disk	Dual-phase – asymmetric	0.020	0.47	Wet 50%H_2-He/wet Ar	750	[17]
$BaCe_{0.65}Zr_{0.2}Y_{0.15}O_{3-\delta}$ (BCZ20Y15) - $Ce_{0.85}Gd_{0.15}O_{2-\delta}$ (GDC15)	disk	Dual-phase – symmetric	0.65	0.27	wet 50%H_2-He/wet Ar	755	[16]
$BaCe_{0.65}Zr_{0.20}Y_{0.15}O_{3-\delta}$ (BCZY)–$Gd_{0.2}Ce_{0.8}O_{2-\delta}$ (GDC) - *(BCZY-GDC)*	disk	Dual-phase – asymmetric	0.013	0.36	Wet 50%H_2-He/wet Ar	750	This work
$BaCe_{0.85}Tb_{0.05}Zr_{0.1}O_{3-\delta}$ (BCTZ) - *BCTZ*	disk	Single-phase – asymmetric	0.020	0.35	50%H_2-He/Ar	1000	[46]
Cerate-based							
$SrCe_{0.9}Y_{0.1}O_{3-\delta}$-$Ce_{0.8}Sm_{0.2}O_2$ (SCY-SDC)	disk	Dual-phase independently distributed - symmetric	1	0.163	20% H_2 -He/N_2	900	[47]
$SrCe_{0.95}Yb_{0.05}O_{3-\alpha}$ (SCY) - *$SrZr_{0.95}Y_{0.05}O_{3-\alpha}$*	disk	single phase - asymmetric	0.002	$6\cdot10^{-4}$ mol cm^{-2} min^{-1}	H_2-N_2/N_2	680	[22]
$BaCe_{0.8}Y_{0.2}O_{3-\alpha}$ (BCY)	hollow fiber	Single-phase - symmetric	0.4	0.38	25% H2–He / N_2	1050	[48]
$BaCe_{0.85}Tb_{0.05}Co_{0.10}O_{3-\delta}$ (BCTCo) - (BCTCo)	hollow fiber	Single-phase – asymmetric	0.132	0.42	50%H_2-He/N_2	1000	[49]
$BaCe_{0.8}Y_{0.2}O_{3-\delta}$ (BCY)-$Ce_{0.8}Y_{0.2}O_{2-\delta}$ (YDC) - *(BCY-Ni)*	hollow fiber	Dual-phase – asymmetric	0.017	0.566	50%H_2-He/N_2	900	[50]
$SrCe_{0.95}Tm_{0.05}O_{3-\delta}$ (SCTm) - *SCTm*	disk	Single-phase – asymmetric	0.150	$9.37\cdot10^{-8}$ mol $cm^{-2}s^{-1}$	10%H_2-He/Air	900	[42]
$SrCe_{0.95}Y_{0.05}O_{3-\delta}$ (SCY) - *SCY*	disk	Single-phase – asymmetric	0.050	$7.6\cdot10^{-8}$ mol $cm^{-2}s^{-1}$	80%H_2-He/Ar	950	[43]
$La_{0.5}Ce_{0.5}O_{2-\delta}$ (LDC) - *LDC*	disk	Single-phase – asymmetric	0.030	$2.6\cdot10^{-8}$ mol $cm^{-2}s^{-1}$	20%H_2-He-3%H_2O/Ar	900	[44]

$BaCe_{0.9}Y_{0.1}O_{3-\delta}$ - *ZrO_2*	disk	Dual phase - asymmetric	Dense	0.17	10%H_2-N_2/Ar	800	[51]
Ferrite-based							
$SrCe_{0.95}Fe_{0.05}O_{3-\delta}$-$SrFe_{0.95}Ce_{0.05}O_{3-\delta}$ (SCF-SFC)	disk	Dual phase - symmetric	0.7	0.38	40%H_2-N_2/wet Ar	940	[52]
$Ce_{0.90}Gd_{0.10}O_{2-\delta}$ - $SrCe_{0.95}Fe_{0.05}O_{3-\delta}$ - $SrFe_{0.95}Ce_{0.05}O_{3-\delta}$	disk	Triple phase - symmetric	0.7	0.54	40%H_2-N_2/wet Ar	940	[53]
$BaCo_{0.4}Fe_{0.4}Zr_{0.1}Y_{0.1}O_{3-\delta}$ (BCFZY)	disk	single-phase symmetric	0.65	1.02	10%H_2-N_2/Ar	950	[54]
Tungstate-based							
$La_{5.5}(W_{0.6}Mo_{0.4})_{0.95}Pd_{0.05}O_{11.25-\delta}$	disk	single-phase symmetric	0.25	0.4	50%H_2-He/N_2	800	[55]
$La_{28-x}W_{4+x}O_{54+\delta}$ (LaWO) – *LaWO*	disk	Single phase - asymmetric	0.030	0.4	50% H_2 -He/Air-H_2O	825	[56]

Conclusions

An innovative ceramic membrane architecture for hydrogen separation was manufactured and investigated for the first time. A hierarchically-structured BCZY-GDC membrane was successfully obtained in a two-step process, coupling freeze casting with screen printing for the manufacturing of the porous support and the dense active layer respectively. The production of the latter, in particular, required a carful optimization of the screen printing ink in terms of nature and amount of deflocculant and type of starting BCZY powders. It was found that BCZY-GDC powder is stabilized by GTO, for concentrations equal to $1x10^{-3}$ g/m^2_{powder} of dispersant, through a steric mechanism. On the other hand, only the use of a coarse BCZY powder in the screen printing ink leaded to the production of a crack-free, dense layer onto the freeze cast supports. The optimization of the whole ceramic process allowed to finally obtain hierarchically-structured BCZY-GDC membranes constituted by a porous support with 50% of aligned porosity and a 13 ± 3 μm thick dense layer with residual porosity of 1.5 ± 0.9 %. The registered mechanical properties, i.e. microhardness (452 ± 95 HV) and compressive strength (20.6 ± 5.6 MPa), were considered acceptable for practical applications. Hydrogen permeation tests were conducted in the 350-750 °C temperatures range using three different feed compositions. Promising J_{H2} values of 0.36 and 0.42 mL min^{-1} cm^{-2} at 750°C, using a feed stream with 50 and 80% H_2 in He (H_2 %vol.) respectively, were obtained reducing the thickness of the porous support. It was demonstrated that this kind of architecture, differently from tape cast one, allows to select the desired thickness of the porous layer based on the required mechanical resistance without substantial losses in hydrogen permeation performances.

In conclusion, this study highlights for the first time the potentialities of hierarchically-structured BCZY-GDC membranes for hydrogen separation. The development of this innovative architecture will allow to facilitate the infiltration process of the catalysts and/or wash-coating suspensions into the porous side to produce “reactive membranes”. Moreover, the use of water-based suspensions makes freeze casting more environmentally friendly and less time and energy consuming compared

to tape casting, which generally involves the use of organic suspensions and pore former agents that need ad-hoc and slow debinding thermal cycles.

Further investigations are still required to assess the predominant key-parameters to improve H_2 permeation of ceramic-ceramic membranes.

Acknowledgments

This work has been funded by the agreement between the Italian Ministry of Economic Development and the Italian National Research Council ‘‘Ricerca di sistema elettrico nazionale’’. The Authors would like to thank Mr Cesare Melandri, Mrs Paola Pinasco and Mrs Guia Guarini for respectively the mechanical tests, porosimetric analyses and gravitational particle size analyses.

References

[1] S. van Renssen, The hydrogen solution?, Nat. Clim. Chang. 10 (2020) 799–801. https://doi.org/10.1038/s41558-020-0891-0.

[2] B.E. Lebrouhi, J.J. Djoupo, B. Lamrani, K. Benabdelaziz, T. Kousksou, Global hydrogen development - A technological and geopolitical overview, International Journal of Hydrogen Energy. 47 (2022) 7016–7048. https://doi.org/10.1016/j.ijhydene.2021.12.076.

[3] P. Nikolaidis, A. Poullikkas, A comparative overview of hydrogen production processes, Renewable and Sustainable Energy Reviews. 67 (2017) 597–611. https://doi.org/10.1016/j.rser.2016.09.044.

[4] J. De Maron, R. Mafessanti, P. Gramazio, E. Orfei, A. Fasolini, F. Basile, H2 Production by Methane Oxy-Reforming: Effect of Catalyst Pretreatment on the Properties and Activity of Rh-Ce0.5Zr0.5O2 Synthetized by Microemulsion, Nanomaterials. 13 (2023) 53. https://doi.org/10.3390/nano13010053.

[5] A. Inayat, A. Fasolini, F. Basile, D. Fridrichova, P. Lestinsky, Chemical recycling of waste polystyrene by thermo-catalytic pyrolysis: A description for different feedstocks, catalysts and operation modes, Polymer Degradation and Stability. 201 (2022) 109981. https://doi.org/10.1016/j.polymdegradstab.2022.109981.

[6] A. Fasolini, S. Ruggieri, C. Femoni, F. Basile, Highly Active Catalysts Based on the Rh4(CO)12 Cluster Supported on Ce0.5Zr0.5 and Zr Oxides for Low-Temperature Methane Steam Reforming, Catalysts. 9 (2019) 800. https://doi.org/10.3390/catal9100800.

[7] A. Fasolini, S. Abate, D. Barbera, G. Centi, F. Basile, Pure H2 production by methane oxy-reforming over Rh-Mg-Al hydrotalcite-derived catalysts coupled with a Pd membrane, Applied Catalysis A: General. 581 (2019) 91–102. https://doi.org/10.1016/j.apcata.2019.05.024.

[8] G. Bernardo, T. Araújo, T. da Silva Lopes, J. Sousa, A. Mendes, Recent advances in membrane technologies for hydrogen purification, International Journal of Hydrogen Energy. 45 (2020) 7313–7338. https://doi.org/10.1016/j.ijhydene.2019.06.162.

[9] H. Cheng, Dual-Phase Mixed Protonic-Electronic Conducting Hydrogen Separation Membranes: A Review, Membranes. 12 (2022) 647. https://doi.org/10.3390/membranes12070647.
[10] M. Taghizadeh, F. Aghili, Recent advances in membrane reactors for hydrogen production by steam reforming of ethanol as a renewable resource, Reviews in Chemical Engineering. 35 (2019) 377–392. https://doi.org/10.1515/revce-2017-0083.
[11] W. Deibert, M.E. Ivanova, S. Baumann, O. Guillon, W.A. Meulenberg, Ion-conducting ceramic membrane reactors for high-temperature applications, Journal of Membrane Science. 543 (2017) 79–97. https://doi.org/10.1016/j.memsci.2017.08.016.
[12] I. Kalaitzidou, A. Katsaounis, T. Norby, C.G. Vayenas, Electrochemical promotion of the hydrogenation of CO2 on Ru deposited on a BZY proton conductor, Journal of Catalysis. 331 (2015) 98–109. https://doi.org/10.1016/j.jcat.2015.08.023.
[13] E. Ruiz, P.J. Martínez, Á. Morales, G. San Vicente, G. de Diego, J.M. Sánchez, Electrochemically assisted synthesis of fuels by CO2 hydrogenation over Fe in a bench scale solid electrolyte membrane reactor, Catalysis Today. 268 (2016) 46–59. https://doi.org/10.1016/j.cattod.2016.02.025.
[14] Y.S. Lin, Inorganic Membranes for Process Intensification: Challenges and Perspective, Ind. Eng. Chem. Res. 58 (2019) 5787–5796. https://doi.org/10.1021/acs.iecr.8b04539.
[15] D. Montaleone, E. Mercadelli, A. Gondolini, P. Pinasco, A. Sanson, On the compatibility of dual phase BaCe0.65Zr0.2Y0.15O3-based membrane for hydrogen separation application, Ceramics International. 43 (2017) 10151–10157. https://doi.org/10.1016/j.ceramint.2017.05.039.
[16] E. Rebollo, C. Mortalò, S. Escolástico, S. Boldrini, S. Barison, J. M. Serra, M. Fabrizio, Exceptional hydrogen permeation of all-ceramic composite robust membranes based on BaCe 0.65 Zr 0.20 Y 0.15 O 3−δ and Y- or Gd-doped ceria, Energy & Environmental Science. 8 (2015) 3675–3686. https://doi.org/10.1039/C5EE01793A.
[17] E. Mercadelli, A. Gondolini, D. Montaleone, P. Pinasco, S. Escolástico, J.M. Serra, A. Sanson, Production strategies of asymmetric BaCe0.65Zr0.20Y0.15O3-δ – Ce0.8Gd0.2O2-δ membrane for hydrogen separation, International Journal of Hydrogen Energy. 45 (2020) 7468–7478. https://doi.org/10.1016/j.ijhydene.2019.03.148.
[18] D. Montaleone, E. Mercadelli, S. Escolástico, A. Gondolini, J.M. Serra, A. Sanson, All-ceramic asymmetric membranes with superior hydrogen permeation, J. Mater. Chem. A. 6 (2018) 15718–15727. https://doi.org/10.1039/C8TA04764B.
[19] E. Mercadelli, A. Gondolini, M. Ardit, G. Cruciani, C. Melandri, S. Escolástico, J.M. Serra, A. Sanson, Chemical and mechanical stability of BCZY-GDC membranes for hydrogen separation, Separation and Purification Technology. 289 (2022) 120795. https://doi.org/10.1016/j.seppur.2022.120795.
[20] C. Mortalò, E. Rebollo, S. Escolástico, S. Deambrosis, K. Haas-Santo, M. Rancan, R. Dittmeyer, L. Armelao, M. Fabrizio, Enhanced sulfur tolerance of BaCe0.65Zr0.20Y0.15O3-δ-Ce0.85Gd0.15O2-δ composite for hydrogen separation membranes, Journal of Membrane Science. 564 (2018) 123–132. https://doi.org/10.1016/j.memsci.2018.07.015.
[21] E. Mercadelli, D. Montaleone, A. Gondolini, P. Pinasco, A. Sanson, Tape-cast asymmetric membranes for hydrogen separation, Ceramics International. 43 (2017) 8010–8017. https://doi.org/10.1016/j.ceramint.2017.03.099.
[22] S. Hamakawa, L. Li, A. Li, E. Iglesia, Synthesis and hydrogen permeation properties of membranes based on dense SrCe0.95Yb0.05O3−α thin films, Solid State Ionics. 148 (2002) 71–81. https://doi.org/10.1016/S0167-2738(02)00047-4.
[23] Freeze casting â€“ A review of processing, microstructure and properties via the open data repository, FreezeCasting.net | Elsevier Enhanced Reader, (n.d.). https://doi.org/10.1016/j.pmatsci.2018.01.001.

[24] F. Schulze-Küppers, U.V. Unije, H. Blank, M. Balaguer, S. Baumann, R. Mücke, W.A. Meulenberg, Comparison of freeze-dried and tape-cast support microstructure on high-flux oxygen transport membrane performance, Journal of Membrane Science. 564 (2018) 218–226. https://doi.org/10.1016/j.memsci.2018.07.028.
[25] C. Gaudillere, J. Garcia-Fayos, J.M. Serra, Enhancing oxygen permeation through hierarchically-structured perovskite membranes elaborated by freeze-casting, J. Mater. Chem. A. 2 (2014) 3828. https://doi.org/10.1039/c3ta14069e.
[26] A. Gondolini, E. Mercadelli, S. Casadio, A. Sanson, Freeze cast support for hydrogen separation membrane, Journal of the European Ceramic Society. 42 (2022) 1053–1060. https://doi.org/10.1016/j.jeurceramsoc.2021.10.063.
[27] A. Gondolini, E. Mercadelli, G. Constantin, L. Dessemond, V. Yurkiv, R. Costa, A. Sanson, On the manufacturing of low temperature activated Sr0.9La0.1TiO3-δ-Ce1-xGdxO2-δ anodes for solid oxide fuel cell, Journal of the European Ceramic Society. 38 (2018) 153–161. https://doi.org/10.1016/j.jeurceramsoc.2017.07.035.
[28] A. Gondolini, N. Sangiorgi, A. Sangiorgi, A. Sanson, Photoelectrochemical Hydrogen Production by Screen-Printed Copper Oxide Electrodes, Energies. 14 (2021) 2942. https://doi.org/10.3390/en14102942.
[29] R. Moreno, Better ceramics through colloid chemistry, Journal of the European Ceramic Society. 40 (2020) 559–587. https://doi.org/10.1016/j.jeurceramsoc.2019.10.014.
[30] A. Gondolini, A. Fasolini, E. Mercadelli, F. Basile, A. Sanson, Freeze cast porous membrane catalyst for hydrogen production via oxy-reforming, Fuel Processing Technology. (2020) 106658. https://doi.org/10.1016/j.fuproc.2020.106658.
[31] M. Cai, S. Liu, K. Efimov, J. Caro, A. Feldhoff, H. Wang, Preparation and hydrogen permeation of BaCe0.95Nd0.05O3− membranes, Journal of Membrane Science. 343 (2009) 90–96. https://doi.org/10.1016/j.memsci.2009.07.011.
[32] H. Matsumoto, T. Shimura, H. Iwahara, T. Higuchi, K. Yashiro, A. Kaimai, T. Kawada, J. Mizusaki, Hydrogen separation using proton-conducting perovskites, Journal of Alloys and Compounds. 408–412 (2006) 456–462. https://doi.org/10.1016/j.jallcom.2004.12.093.
[33] C. Gaudillere, J.M. Serra, Freeze-casting: Fabrication of highly porous and hierarchical ceramic supports for energy applications, Boletín de La Sociedad Española de Cerámica y Vidrio. 55 (2016) 45–54. https://doi.org/10.1016/j.bsecv.2016.02.002.
[34] X. Shao, Z. Wang, S. Xu, K. Xie, X. Hu, D. Dong, G. Parkinson, C.-Z. Li, Microchannel structure of ceramic membranes for oxygen separation, Journal of the European Ceramic Society. 36 (2016) 3193–3199. https://doi.org/10.1016/j.jeurceramsoc.2016.05.005.
[35] S. Escolástico, C. Solís, J.M. Serra, Study of hydrogen permeation in (La5/6Nd1/6)5.5WO12-δ membranes, Solid State Ionics. 216 (2012) 31–35. https://doi.org/10.1016/j.ssi.2011.11.004.
[36] S. Escolástico, M. Ivanova, C. Solís, S. Roitsch, W.A. Meulenberg, J.M. Serra, Improvement of transport properties and hydrogen permeation of chemically-stable proton-conducting oxides based on the system BaZr1-x-yYxMyO3-δ, RSC Adv. 2 (2012) 4932. https://doi.org/10.1039/c2ra20214j.
[37] S. Escolástico, C. Solís, T. Scherb, G. Schumacher, J.M. Serra, Hydrogen separation in La5.5WO11.25−δ membranes, Journal of Membrane Science. 444 (2013) 276–284. https://doi.org/10.1016/j.memsci.2013.05.005.
[38] S. Escolástico, C. Solís, J.M. Serra, Hydrogen separation and stability study of ceramic membranes based on the system Nd5LnWO12, International Journal of Hydrogen Energy. 36 (2011) 11946–11954. https://doi.org/10.1016/j.ijhydene.2011.06.026.
[39] S. Escolastico, J. Seeger, S. Roitsch, M. Ivanova, W.A. Meulenberg, José.M. Serra, Enhanced H_2 Separation through Mixed Proton-Electron Conducting Membranes Based on $La_{5.5}W_{0.8}M_{0.2}O_{11.25-\delta}$, ChemSusChem. 6 (2013) 1523–1532. https://doi.org/10.1002/cssc.201300091.
[40] J. Li, H. Yoon, E.D. Wachsman, Hydrogen permeation through thin supported SrCe0.7Zr0.2Eu0.1O3−δ membranes; dependence of flux on defect equilibria and operating

conditions, Journal of Membrane Science. 381 (2011) 126–131. https://doi.org/10.1016/j.memsci.2011.07.032.
[41] I.-M. Hung, Y.-J. Chiang, J.S.-C. Jang, J.-C. Lin, S.-W. Lee, J.-K. Chang, C.-S. Hsi, The proton conduction and hydrogen permeation characteristic of Sr(Ce0.6Zr0.4)0.85Y0.15O3−δ ceramic separation membrane, Journal of the European Ceramic Society. 35 (2015) 163–170. https://doi.org/10.1016/j.jeurceramsoc.2014.08.019.
[42] S. Cheng, V.K. Gupta, J.Y.S. Lin, Synthesis and hydrogen permeation properties of asymmetric proton-conducting ceramic membranes, Solid State Ionics. 176 (2005) 2653–2662. https://doi.org/10.1016/j.ssi.2005.07.005.
[43] S. Zhan, X. Zhu, B. Ji, W. Wang, X. Zhang, J. Wang, W. Yang, L. Lin, Preparation and hydrogen permeation of SrCe0.95Y0.05O3−δ asymmetrical membranes, Journal of Membrane Science. 340 (2009) 241–248. https://doi.org/10.1016/j.memsci.2009.05.037.
[44] Z. Zhu, L. Yan, H. Liu, W. Sun, Q. Zhang, W. Liu, A mixed electronic and protonic conducting hydrogen separation membrane with asymmetric structure, International Journal of Hydrogen Energy. 37 (2012) 12708–12713. https://doi.org/10.1016/j.ijhydene.2012.06.033.
[45] T. Oh, H. Yoon, J. Li, E.D. Wachsman, Hydrogen permeation through thin supported SrZr0.2Ce0.8−xEuxO3−δ membranes, Journal of Membrane Science. 345 (2009) 1–4. https://doi.org/10.1016/j.memsci.2009.08.031.
[46] Y. Wei, J. Xue, H. Wang, J. Caro, Hydrogen permeability and stability of BaCe0.85Tb0.05Zr0.1O3−δ asymmetric membranes, Journal of Membrane Science. 488 (2015) 173–181. https://doi.org/10.1016/j.memsci.2015.04.035.
[47] B. Meng, H. Wang, H. Cheng, X. Wang, X. Meng, J. Sunarso, X. Tan, S. Liu, Hydrogen permeation performance of dual-phase protonic-electronic conducting ceramic membrane with regular and independent transport channels, Separation and Purification Technology. 213 (2019) 515–523. https://doi.org/10.1016/j.seppur.2018.12.068.
[48] X. Tan, X. Tan, N. Yang, B. Meng, K. Zhang, S. Liu, High performance BaCe0.8Y0.2O3−a (BCY) hollow fibre membranes for hydrogen permeation, Ceramics International. 40 (2014) 3131–3138. https://doi.org/10.1016/j.ceramint.2013.09.132.
[49] J. Song, J. Kang, X. Tan, B. Meng, S. Liu, Proton conducting perovskite hollow fibre membranes with surface catalytic modification for enhanced hydrogen separation, Journal of the European Ceramic Society. 36 (2016) 1669–1677. https://doi.org/10.1016/j.jeurceramsoc.2016.01.006.
[50] H. Cheng, X. Wang, X. Meng, B. Meng, J. Sunarso, X. Tan, L. Liu, S. Liu, Dual-layer BaCe0.8Y0.2O3-δ-Ce0.8Y0.2O2-δ/BaCe0.8Y0.2O3-δ-Ni hollow fiber membranes for H2 separation, Journal of Membrane Science. 601 (2020) 117801. https://doi.org/10.1016/j.memsci.2019.117801.
[51] J.-H. Kim, Y.-M. Kang, B.-G. Kim, S.-H. Lee, K.-T. Hwang, Preparation of dense composite membrane with Ba-cerate conducting oxide and rapidly solidified Zr-based alloy, International Journal of Hydrogen Energy. 36 (2011) 10129–10135. https://doi.org/10.1016/j.ijhydene.2011.02.145.
[52] L. Jia, S. Ashtiani, F. Liang, G. He, H. Jiang, Hydrogen permeation through dual-phase ceramic membrane derived from automatic phase-separation of SrCe0.50Fe0.50O3-δ precursor, International Journal of Hydrogen Energy. 45 (2020) 4625–4634. https://doi.org/10.1016/j.ijhydene.2019.11.241.
[53] L. Jia, M. Liu, X. Xu, W. Dong, H. Jiang, Gd-doped ceria enhanced triple-conducting membrane for efficient hydrogen separation, Separation and Purification Technology. 256 (2021) 117798. https://doi.org/10.1016/j.seppur.2020.117798.
[54] D. Zhang, X. Zhang, X. Zhou, Y. Song, Y. Jiang, B. Lin, Phase stability and hydrogen permeation performance of BaCo0·4Fe0·4Zr0·1Y0·1O3-δ ceramic membranes, Ceramics International. 48 (2022) 9946–9954. https://doi.org/10.1016/j.ceramint.2021.12.200.

[55] G. Weng, K. Ouyang, X. Lin, S. Wen, Y. Zhou, S. Lei, J. Xue, H. Wang, Enhanced Hydrogen Permeability of Mixed Protonic–Electronic Conducting Membranes through an In-Situ Exsolution Strategy, Advanced Functional Materials. 32 (2022) 2205255. https://doi.org/10.1002/adfm.202205255.
[56] M.E. Ivanova, W. Deibert, D. Marcano, S. Escolástico, G. Mauer, W.A. Meulenberg, M. Bram, J.M. Serra, R. Vaßen, O. Guillon, Lanthanum tungstate membranes for H2 extraction and CO2 utilization: Fabrication strategies based on sequential tape casting and plasma-spray physical vapor deposition, Separation and Purification Technology. 219 (2019) 100–112. https://doi.org/10.1016/j.seppur.2019.03.015.